ARTICLE

Enhancing plasmonic hot carrier generation by strong coupling of multiple resonant modes

Received 00th January 20xx,
Accepted 00th January 20xx

DOI: 10.1039/x0xx00000x

Yat Lam Wong,[a] Huaping Jia,[a,b] Aoqun Jian,[b] Dangyuan Lei,[c] Abdel I. El Abed,[d] and Xuming Zhang *,[a]

Plasmon-induced hot carriers have recently attracted intensive research, but the energy efficiency in the visible light is often low due to the short lifetime of hot carriers and the limited optical absorption of plasmonic architectures. To boost the generation of hot carriers, here we propose to exert multiple plasmonic resonant modes and their strong coupling using a metal-dielectric-metal (MDM) nanocavity that consists of an Au nanohole array (AuNHA), a TiO_2 thin film and an Au reflector. Unlike common MDM structures, in addition to the Fabry-Pérot mode in the dielectric layer, the AuNHA as the top layer is special since it excites the localized surface plasmon resonance (LSPR) mode in the Au nanoholes and launches the gap surface plasmon polariton (GSPP) mode in the Au reflector surface. The spatial field overlapping of three resonance modes enables strong mode coupling by optimizing the TiO_2 thickness, leading to notably enhanced average IPCE (~1.5%) and broadband photocurrent (170 $\mu A \cdot cm^{-2}$). This MDM structure would be useful for photochemistry and photovoltaics using sunlight.

Introduction

Surface plasmon resonance (SPR) excited on metal nanostructures can drastically enhance the interaction of light with matter.[1] Recently, array of nanoholes perforated on an ultrathin metallic film has demonstrated intriguing plasmonic properties as compared to its complementary counterpart – array of nanoparticles.[2-4] A prominent feature of the plasmonic nanohole array (NHA) is the structural continuity, which enables the excitation of surface plasmon polariton (SPP) at two interfaces of metal film and also facilitates the direct electrical connection of photocurrent. In case the plasmonic film is in the ultrathin regime, the SPP modes on two interfaces would couple together to form a lossy short-range SPP mode, which is prone to the nonradiative dissipation of energy in the film.[5,6] Nevertheless, the magnitude and broadness of the absorption are limited for an ultrathin plasmonic NHA. Effort has been made to maximize the absorption by integrating plasmonic structures into the conventional metal-dielectric-metal (MDM) structure, which exhibits multiband absorption from the LSPR and the cavity mode.[7-9] In the system with multiple resonances, modes with the same energy in their uncoupled states are often detuned and hybridized into new repulsive states.[10, 11] The magnitude of the detuning is a direct indication of the strength of the mutual interaction of the resonance modes. This concept is vital to harnessing the spontaneous emission of an emitter in studying the cavity quantum electrodynamics.[12, 13] In addition to the optical absorption, we are also interested in the hot carrier generation as a result of the plasmonic absorption. Energy acquired from the optical absorption can transfer to excitation of an electron-hole pair through Landau damping. [14] The generated carriers are generally referred as “hot” carrier due to the extended tail of Fermi distribution to a higher energy as if the system behaves in a higher effective temperature. [14] Unfortunately, the lifetime of hot carriers is usually in the order of tens of femtosecond before they undergo relaxation through electron-electron scattering, so proper strategy for charge separation is crucial to prolong the carriers’ lifetime. [15] Many efforts have been made to engineer the hot carrier generation by the rectification effect of the metal-dielectric junction. [16] Recently, coupling effect between resonance modes have found to be strongly alter the hot carrier generation associated with the plasmon resonance. [17-19] However, only few literatures have discussed the influence of the mode coupling effects in the structure on the plasmon-induced hot carrier generation. [17-19] These literatures have demonstrated an enhancement of plasmonic hot carrier generation in the strong coupling regime. The underlying mechanism of the enhancement is suggested to be the modulation of radiative damping resulted from the coherent energy exchange within strongly interacted resonators. [19] Nevertheless, two of these studies only explore the mode coupling effects between plasmonic particles and cavity in the particle/dielectric/metal reflector system. [17,18] The

[a] *Department of Applied Physics, The Hong Kong Polytechnic University, Hong Kong, P.R. China*
E-mail: apzhang@polyu.edu.hk, dangylei@cityu.edu.hk
[b] *MircoNano System Research Center, College of Information and Computer Science, Taiyuan University of Technology, Taiyuan, Shanxi 0303024, P.R. China*
[c] *Department of Materials Science and Engineering, City University of Hong Kong, Hong Kong, P.R. China*
[d] *Laboratoire Lumière Matière et Interfaces (LuMIn), Institut d’Alembert, Ecole Normale Supérieure Paris Saclay, CentraleSupélec, CNRS, Université Paris-Saclay, 61 avenue du PrésidentWilson, 94235 Cachan, France*

†Electronic Supplementary Information (ESI) available: SEM image, AFM, reflection spectra, absorption spectra, GSPP mode, scattering cross-section spectra, IPCE spectra, local electric field spectra. See DOI: 10.1039/x0xx00000x

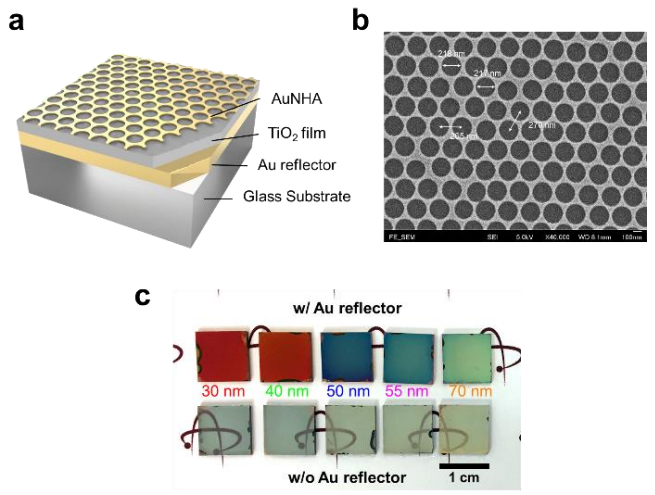

Fig. 1. (a) Schematic diagram of the AuNHA/TiO_2/Au metal-dielectric-metal (MDM) absorber proposed in this work; and (b) the scanning electron microscopic (SEM) image of the fabricated Au nanohole array (AuNHA), the hole diameters are 217 and 218 nm and the interhole distances are 265 and 270 nm as marked in the SEM. (c) Photographs of the fabricated absorbers with (above) and without (below) Au back reflector and having the TiO_2 thicknesses of 30, 40, 50, 55, and 70 nm (from left to right), respectively

plasmonic hot carrier generation in more complex coupling systems has yet to be examined carefully.

MDM architectures patterned with metallic grating enable SPP modes on the metal-dielectric interface due to the compensation of the momentum mismatch by the ordered nature of the structures. [11] If the metallic grating in the MDM structure also supports SPP modes, the SPPs on both metal-dielectric interfaces can couple together to form a guided mode within the dielectric layer, namely gap-SPP (GSPP) mode. [20] The symmetric coupling of two SPPs in a nearly lossless dielectric medium results in a high confinement of energy, which we consider to be essential in plasmonic hot carrier generation. However, studies that particularly focus on this issue have yet to be done.

In this work, we propose a plasmonic absorber with the MDM structure of AuNHA/TiO_2/Au, which consists of an ultrathin Au nanohole array (AuNHA), a TiO_2 layer and an Au reflector (from top to bottom, see Figure 1a). Three absorption bands corresponding to the cavity mode, the gap-SPP (GSPP) mode, and the LSPR mode appear over the visible to near infrared range. We will demonstrate the evolution of these modes and the associated plasmon-induced hot carrier generation with respect to the variation of the thickness of TiO_2 layer. The hot carrier generation will be measured by an electrochemical system using the redox couples of Fe^{2+}/Fe^{3+}.

Results and Discussion

Morphological characterization

The AuNHA films in this work are fabricated by using nanosphere lithography (NSL) and reactive ion etching (RIE) (more details in the Experimental Section). Morphological analysis of the AuNHA is done by scanning electron microscopy (SEM) and atomic force microscopy (AFM). The nanoholes are arranged in a hexagonal lattice with the periodicity strictly followed the diameter of the unetched polystyrene spheres (see Fig. 1b). The interhole distance and the hole diameter have the averaged values of 265 nm and 222 nm, respectively, as measured from the SEM and the histogram in Fig. S1,† Supporting Information. Based on the 3-dimensional contour diagram and the profiles of the AFM images (see Fig. S2,† Supporting Information), the period and the thickness of AuNHA are measured to be 260 nm and 32 nm, respectively.

Optical characterization

To investigate the influence of TiO_2 thickness on the optical properties, the AuNHA/TiO_2/Au MDM absorbers with 5 different thicknesses of TiO_2 film are numerically and experimentally studied, with the focus on their optical absorption spectra. In the simulated spectra (Fig. 2a), three absorption peaks are discernible. For simplicity, the peaks with the shortest, middle, and longest wavelengths are marked as “U”, “M”, and “L”, respectively (representing upper, middle and lower). As the thickness of TiO_2 thin film increases from 30 to 70 nm, the peak “U” presents a red shift and the peak “L” has a blue shift. Interestingly, the peak “M” is insensitive to the variation of TiO_2 thickness. Consequently, the peaks “U” and “L” are squeezed toward to the peak “M”, but they are never merged into one. At the optimal TiO_2 thickness of 55 nm, three peaks are closest together. Further increase of the TiO_2 thickness does not cause an overlap of the resonant peaks. Instead, they repel each other and are shifted to opposite directions. For the absorber with the TiO_2 thickness of 70 nm, the “L” peak becomes weak and broad. In the measured absorption spectra (see Fig. 2a), they follow a similar trend with the simulated ones, except that the spectral positions of peak “M” deviate from the corresponding simulated values for the structures with the TiO_2 thickness ≥ 50 nm. The discrepancy can be explained by the energy difference between the simulated and experimental resonant energy of the LSPR mode in the uncoupled state. The uncoupled LSPR mode of AuNHA can be studied by the metal-dielectric (MD) structures that have the AuNHA and the TiO_2 film but no back Au reflector (in short, AuNHA/TiO_2). The calculated spectra show two closely separated peaks, they represent the bonding and anti-bonding LSPR modes of the AuNHA (see Fig. S3†). In the measured spectra, the resonances are broadened and red shifted due to the imperfection of structures fabricated by the NSL technique. Since the experimental uncoupled LSPR energies is much closer to the “L” peaks in the coupled system as compared to the simulated spectra, they may have a stronger mode repulsion and lead to a blueshift of the “M” peak.

Figure 1c shows the photos of the samples of five different TiO_2 thicknesses but with or without the Au back reflector. Some features of the absorption spectra can also be seen by

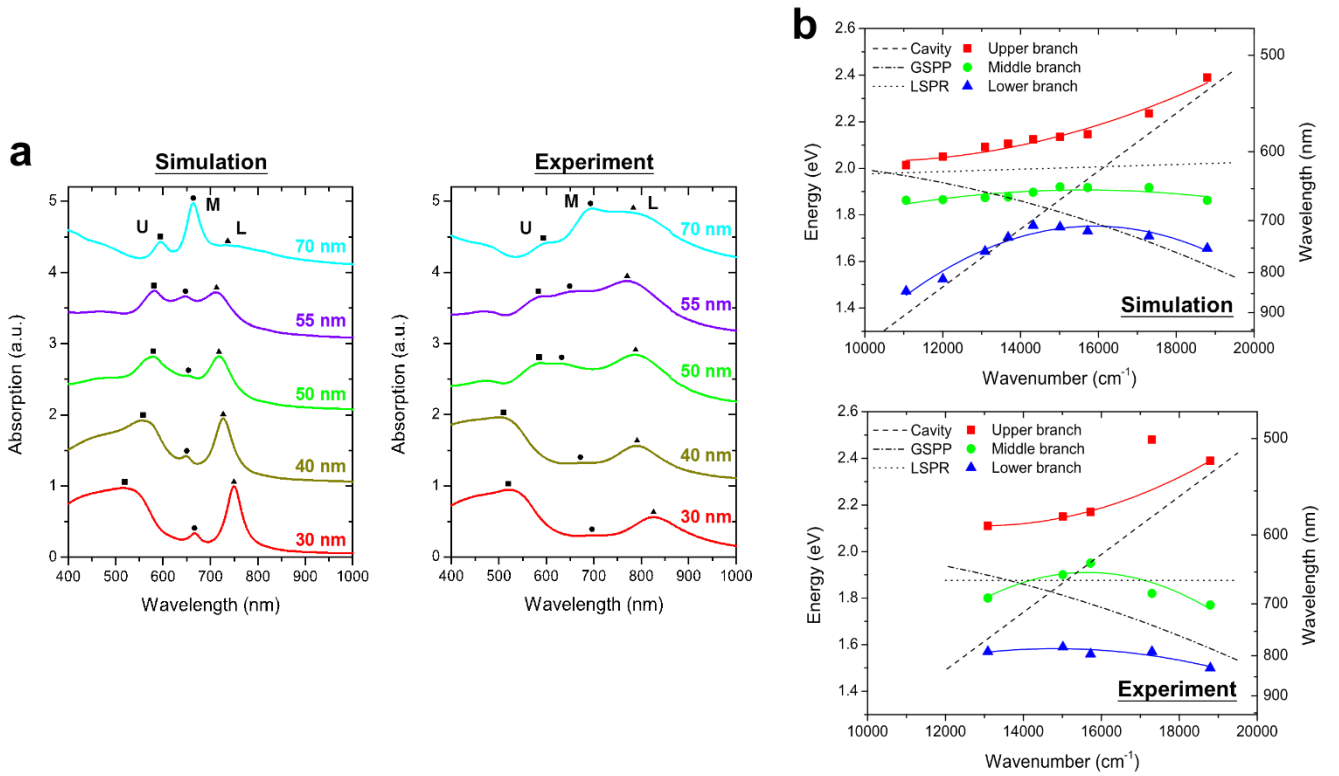

Fig. 2. (a) FDTD simulated and experimentally measured absorption spectra of the AuNHA/TiO_2/Au MDM absorbers with the TiO_2 thicknesses of 30, 40, 50, 55, and 70 nm (from bottom to top). The labels "U", "M", and "L" represent the upper, middle, and lower branches of resonance, respectively. a.u. stands for arbitrary unit. (b) The FDTD simulated and experimental absorption peak positions of three modes as a function of wavenumber of the cavity mode for the AuNHA/TiO_2/Au MDM absorbers. The measured absorption peaks are fitted by the parabolic function to show the trends of three branches. For reference, the uncoupled states of the cavity mode, the LSPR mode of Au nanoholes and the GSPP mode are shown as the dashed, dotted, and dash-dotted lines, respectively. The absorber with the TiO_2 thickness of 55 nm is found to fulfil the global strong coupling condition.

naked eyes from the photos. For instance, the structures without the Au back reflector are highly transparent, though the transparency of the samples gradually decreases with the increase of TiO_2 thickness. For the samples with a back reflector, the color of the samples vary from light red to dark blue, and then to light blue when the TiO_2 thickness is increased from 30 nm to 70 nm. The color change of the absorbers with respect to the TiO_2 thickness directly correlates to the shift and the hybridization of resonances with respect to the TiO_2 thickness illustrated in Fig. 2a.

For analysis, the positions of the absorption peaks of the simulated and experimental spectra for the MDM absorbers are expressed in the unit of eV and plotted against the wavenumber of the cavity mode in Fig. 2b. The wavenumber of cavity mode is estimated from the reflection spectra of the TiO_2/Au/SiO_2 structure (see Fig. S4†). The parabolic fitting curves delineated by the resonances can be easily categorized into three branches: upper, middle and lower branches, which never intersect with each other regardless of the thickness of TiO_2. The evolution of resonant modes with respect to the change of TiO_2 thickness highly resembles the characteristic of strongly coupled oscillators.[13]

Nature of individual modes in the coupled system

For reference, the uncoupled condition of the modes corresponding to three absorption peaks in response to the change of cavity resonance wavenumber with varying TiO_2 thickness are shown in Fig. 2b as the dashed, dash-dotted, and dotted lines to represent the cavity mode, the GSPP mode and the LSPR mode, respectively. They will be discussed one by one as follows.

Regarding the cavity mode (dashed line in Fig. 2b), it is most sensitive to the variation of TiO_2 thickness. To estimate the cavity resonance on its uncoupled condition, we choose a bilayer structure with a TiO_2 film and a 100-nm Au film (from upper to lower, TiO_2/Au in short) and calculate the optical response by the transfer matrix method.[14] The cavity resonance in the TiO_2 film can be read from the reflection dips or the corresponding maxima in the reflection coefficient spectra (see Fig. S4†). Generally speaking, the energy of the cavity resonance is redshifted dramatically with the increase of the TiO_2 thickness, and the resonance at large TiO_2 thickness is broad and weak, which well match the trend in the coupled system. The suppression of reflection is mainly contributed by the Fabry-Pérot-like resonance. Two factors cause the cancellation

of reflected light, the phase difference due to the imaginary dielectric function of Au and the phase change in the dielectric film.[17,21,22]

Regarding the GSPP mode, it is the only one among the three modes that causes a blue shift of the resonant peak in the MDM absorber (dash-dotted line in Fig. 2b) as it is guided in the dielectric layer sandwiched by two metallic films.[23] The dispersion relation of the GSPP mode for the MDM structure on the uncoupled condition can be calculated using the equations (S1) and (S2) in the Supporting Information. It is well known that the in-plane wavevector of the SPP mode at the single metal/dielectric interface never matches the wavevector of light at any frequencies, and so the SPP mode cannot be excited unless this mismatch is compensated. Similarly, the GSPP mode cannot be directly coupled from the free-space light without the assistance of a grating or the presence of scattering centers.[24,25] Nevertheless, the AuNHA in the absorber acts effectively as a grating to provide additional momentum for the excitation of GSPP.[26] The dispersion relation of the GSPP mode for the MDM absorbers with various TiO_2 thicknesses and the momentum provided by grating coupling are both plotted in Fig. S5†. As the intersections in the plot represent the resonance energies of GSPP mode enabled by grating coupling, it can be seen from Fig. S5 that the energy of GSPP is blue-shifted with the increase of TiO_2 thickness, this trend is consistent with the trends in both the FDTD and experimental spectra of the coupled system. The formation of GSPP can be depicted by the coupling between the SPP modes propagating at two dielectric/metal interfaces through their evanescent fields.[27] The GSPP is analogous to the coupled SPP mode supported in an ultrathin AuNHA, though the coupled SPP is usually formed by the anti-symmetrical coupling with a highly lossy characteristic, while the GSPP is formed by the symmetrical coupling with a long propagation length.[20,28] For a deeper understanding of the GSPP mode in the proposed MDM absorber, we conduct the FDTD analysis of the MDM absorber with short-range ordered nanoholes. Through the electrodynamic simulation, the propagation of GSPP mode confined within the TiO_2 layer can be clearly visualized in both the frequency and time-domain manners. Detailed discussions are presented in Supporting Discussion 1, Supporting Information. †

Regarding the LSPR mode, its resonance is supported by the nanoholes of the AuNHA layer (dotted line in Fig. 2b). Here, we assume that the resonance of nanoholes in the MDM structure follows the resonance of an AuNHA on a layer of TiO_2 as already shown in Fig. S4.† But this assumption cannot always be appropriate because the coupling effect between the AuNHA and its own image induced by the back reflector alters the resonance energy, especially when the thickness of TiO_2 is thin.[29-31] To demonstrate the shift of resonance under SPR-image coupling effect, we alternatively study the decoupled SPR using a special MDM system that has a top Au film perforated with only one nanohole (diameter 220 nm), a middle TiO_2 layer and an Au back reflector. Based on the FDTD simulated scattering spectra of the structure in Fig. S6, † the SPR peak of the single-hole system is gradually redshifted with the increase of the TiO_2 thickness. In both cases, the SPR of the AuNHA and the single nanohole show a relatively stable shift of resonance energy in response to the change of the TiO_2 thickness as compared to the other two modes. Nevertheless, we decide to use the resonance of an AuNHA on a layer of TiO_2 to interpret the LSPR resonance in the coupled system as the SPR in an ordered lattice is fundamentally different from an isolated structure.[32]

Strong coupling condition

Anti-crossing behaviour can be observed in Fig. 2b, indicating the existence of modal strong coupling. The fulfilment of strong coupling condition can be evaluated by the linewidth and the energy splitting of the resonances using the relationship $\Omega > (\gamma_U + \gamma_L)/2$, here Ω is the energy splitting, γ_U and γ_L are the linewidths of the upper and lower branch resonances, respectively.[33] In a more complicated system that involves the hybridization of three modes, the criterion can be adapted to a global strong coupling condition as

$$\Omega_{U\text{-}L} > \gamma_M > (\gamma_M + \gamma_{U,L})/2 \quad (1)$$

where Ω_{U-L} refers to the splitting between the upper and lower branches, and γ_M denotes the linewidth of the middle branch, and $\gamma_{U,L}$ represents either γ_U or γ_L.[34] The global minimum of splitting occurs when the MDM absorber has the TiO_2 thickness of 55 nm (this absorber is named as MDM55 hereafter), which will be used to analyze the strong coupling condition. To obtain the linewidth of resonances, multiple Lorentzian fits are implemented on the simulated and experimented absorption spectra as illustrated in Fig. S7. † As summarized in Table 1, the experimental spectra give γ_U = 278 meV, γ_M = 509 meV, and γ_L = 329 meV, whereas the simulated spectra yield γ_U = 217 meV, γ_M = 212 meV, and γ_L = 182 meV. The splitting energy Ω_{U-L} is directly extracted from the anti-crossing plots to be 560 meV for the experiment and 400 meV for the simulation. Correspondingly, the parameters $(\gamma_M + \gamma_U)/2$ and $(\gamma_M + \gamma_L)/2$ are 394 and 419 meV for experiment and 215 and 197 meV for simulation. Substituting all the values into Equation (1), one can find that the strong coupling criterion is satisfied in both the experimental and simulated spectra. It should be noted that the parabolic fitting curves in Fig. 2b merely serve to visualize the trend of each branch but without any physical meaning. Ideally, coupled harmonic oscillator model should be used to verify the composition of model coupling in the dispersion diagrams.[17,34]

Table 1. Analysis of strong mode coupling. Ω_{U-L} refers to the splitting between the upper and lower branches, γ_U, γ_M, and γ_L denote the linewidths of the upper branch, the middle branch, and the lower branch, respectively.

	Ω_{U-L}	γ_U	γ_M	γ_L	$(\gamma_M + \gamma_U)/2$	$(\gamma_M + \gamma_L)/2$	Strong coupling condition
Experiment	560	278	509	329	394	419	fulfilled
FDTD	400	217	212	182	215	197	fulfilled

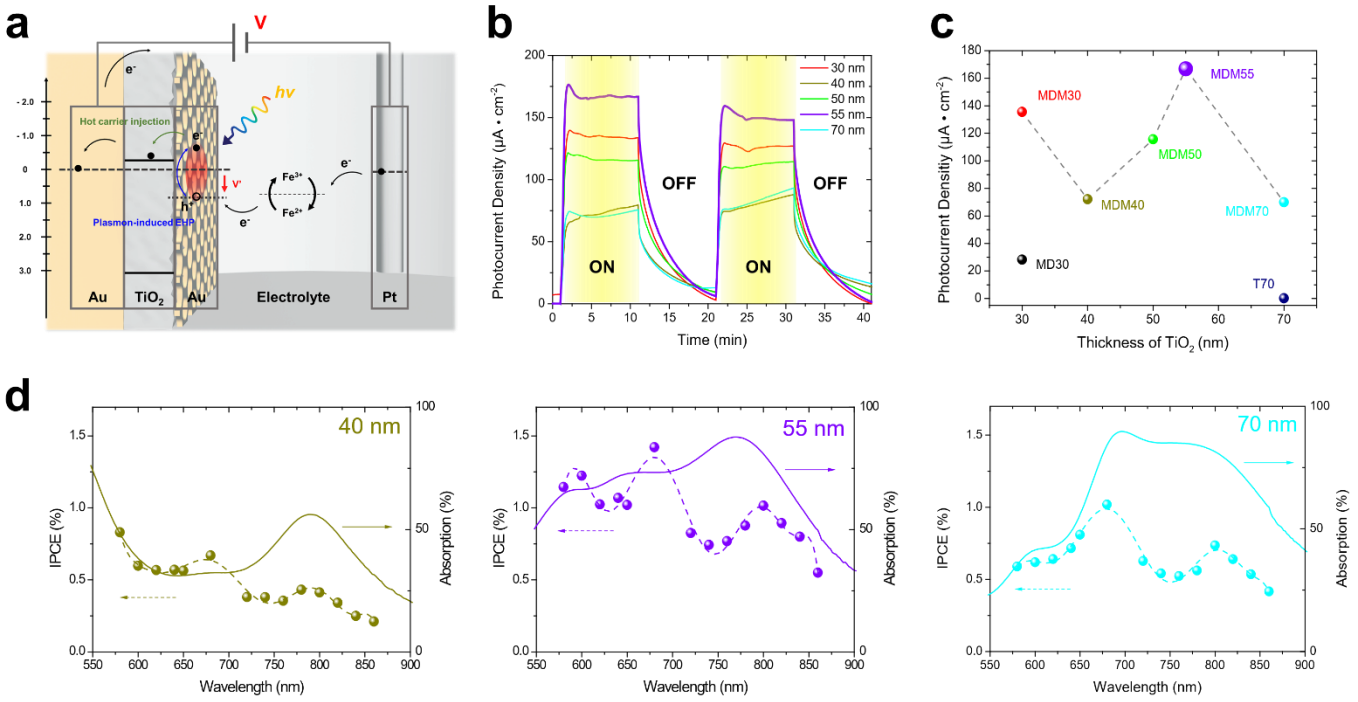

Fig. 3. (a) The schematic diagram of the hot carrier excitation and transport amid the absorber, the Pt electrode, and the Fe^{2+}/Fe^{3+} redox system. (b) The transient photocurrent density of the AuNHA/TiO_2/Au MDM absorbers under the ON/OFF illumination of broadband visible light (wavelength > 490 nm). (c) The stable photocurrent density of the absorbers as a function of the TiO_2 thickness. T70 represents the structure of bare TiO_2 film with the thickness of 70 nm. (d) The IPCE spectra (left axis) and the absorption spectra (right axis) of the MDM structures with the optimized TiO2 thickness (55 nm) and with unoptimized TiO_2 thicknesses (40 and 70 nm). All the photocurrents and IPCEs are measured under the bias voltage of 0.5 V vs. SCE.

Unfortunately, this is unachievable in this system. Because of the inseparable nature between the plasmon resonance of the nanohole array and the GSPP mode in the dielectric layer, the linewidth of the GSPP resonance in the uncoupled state cannot be measured in an unambiguous manner.

Plasmonic hot carrier generation

To quantify the plasmon-induced hot carrier generation using the absorbers, the samples are measured on the photocatalytic efficiency associated with the reduction and oxidation of Fe^{2+} and Fe^{3+}, respectively.[35,36] The carrier generation and transport in the electrochemical system is illustrated in Fig. 3a. The incident photon-to-current conversion efficiencies (IPCEs) for the absorbers with various TiO_2 thicknesses are measured by using 14 monochromatic light sources (see Fig. 3d and Fig. S8†). For easy reference, the experimental absorption spectra of the same absorbers are plotted as well. Reasonable agreement can be seen between the IPCE spectra and the absorption spectra in terms of the peak positions and the general trends. It is worth noting that the TiO_2 thicknesses of 50 nm and 55 nm produce higher IPCE (max. ~1.5%) as compared to the other thicknesses.

Similar dependence of TiO_2 thickness is also observed in the measured photocurrent of the absorbers under the irradiation of broadband visible light (λ > 490 nm). As can be seen from Fig. 3b and c, the MDM55 produces the highest photocurrent density (max. 170 μm·cm^{-2}) in the ON state. For comparison, the second highest photocurrent is recorded from MDM30, which produces 135 μA·cm^{-2}. Consequently, the MDM structure with strong coupling effect enhances the photocurrent by a factor of at least 1.26 as compared to the ones without the strong coupling effect. Moreover, a bare TiO_2 film of 70 nm thick (marked as T70 in Fig. 3c) is prepared and tested as well, which produces only 0.25 μA·cm^{-2}. It is noted that the MDM55 enhances the photocurrent by a factor of 680 as compared to the bare TiO_2 film (70 nm thick).

Both the IPCE and photocurrent measurement show strong correlation between the plasmonic enhancement and the strong coupling effect of the three resonant modes of the AuNHA/TiO_2/Au MDM absorbers. Such an intriguing phenomenon in the strong coupling system was reported by Misawa as well,[17] however the detailed interpretation underneath this phenomenon is elusive. Misawa suggested that the coupled SPR mode has a higher tendency to decay into electron-hole pairs (EHPs) as the dephasing time of SPR mode under the strong coupling condition is shorter than that of the regular SPR mode as proved by the time-resolved photoemission electron microscopy.[11,17,19] The proposed interpretation of the enhancement mechanism is as follows.

Under the strong coupling condition (i.e. MDM55), energy of three resonant modes is able to exchange coherently. As the excitation of GSPP relies on the coupling between the LSPR of AuNHA and the guiding mode in the dielectric layer, coherent energy exchange leads to a preeminent channel for energy confinement or otherwise decaying radiatively into free space for the system in weak coupling regime. [19] The confinement of energy through GSPP mode not only can effectively prolong the plasmon lifetime, but also can increase the generation of plasmonic hot carriers since the SPP is intrinsically prone to decaying non-radiatively.[19] The cavity resonance also plays an important role in maintaining high optical field in the dielectric layer to further facilitate the excitation of LSPR on AuNHA and its coupling with the GSPP mode.

Here, we find that the average optical absorption over the visible and near infrared range reaches maximum when the MDM absorber has the TiO_2 thickness of 55 nm (see Fig. S9†). This further implies that the generation of hot carrier is primarily due to the plasmonic absorption. On the top of this, the intense local field plays another important role in the enhancement of photocatalytic efficiency. Numerous prior studies have already proved that the plasmon-induced hot carrier generation is an electric-field driven event, in which the rate of generation is proportional to the local field enhancement of the SPR.[37-40] To verify the correlation between the strong coupling condition and the local electric field enhancement, the local field intensity in the absorbers is probed by surface enhanced Raman spectroscopy (SERS).[41] The Raman signal intensity is well known to be proportional to the fourth power of the local electric field enhancement, namely $I_{Raman} \propto (E_{loc}/E_0)^4$. Since the TiO_2 material possesses sharp Raman peaks [42] and the TiO_2 film is sandwiched between two metallic structures in the AuNHA/TiO_2/Au MDM structures, these make the SERS signal a suitable indictor of the local field in the structures.[41] The SERS measurements record the strongest enhancement of Raman signals of TiO_2 from MDM55 than all other structures (see Fig. 4). To check whether the SERS of the absorber is contributed by the local field enhancement, we particularly use the FDTD simulation to investigate the electric field enhancement spectra at the middle point of the TiO_2 layer of the absorbers (under three conditions, one strong MDM55 and two weak coupling conditions MDM30 and MDM70) and the absorber without the back reflector (i.e., MD30, see Fig. S10†). One can see that MDM55 presents the largest field enhancement near the excitation laser wavelength (the dashed line in the left panel of Fig. S10†), and the trend of electric field enhancements of the absorbers follows that of the SERS results. It is worth pointing out that the field confinement in our proposed system behaves quite differently from ordinary particle-on-film system in which the field enhancement is maximized by minimizing the thickness of the dielectric (usually within a few nanometers). [30] In Fig. S10, the absorber with the thinnest TiO_2 thickness (i.e. MDM30) has a weak electric field enhancement as compared to the absorber with a thick TiO_2 (i.e. MDM55 or MDM70), indicating that the field enhancement depends on the coupling condition which is sensitive to the TiO_2 thickness as already discussed. Since the evanescent field of the LSPR on the AuNHA needs to extend a fairly long distance (> 30 nm) to interact with the lower film, the field intensity would be significant only if the coupling strength is strong, especially for the GSPP and the cavity mode. For the MDM55, the detuning is small and yet the strong coupling condition is satisfied, the energies of the three resonant mode (i.e., the cavity, the GSPP and the SPR) can exchange reversibly, leading to an enhancement of the weak evanescent field in the dielectric layer as compared to the other case with a large detuning or a weak coupling system.[11] Fig. S11 shows the internal quantum efficiency (IQE) of the MDM absorber with strong coupling effect, the MDM absorber without strong coupling effect (i.e., with weak coupling effect), and the MD absorber (without reflector). The carrier generated from the absorber with the strong mode coupling effect manifests elevated IQE as compared to the structure with weak coupling effect and the structure with mono-plasmon mode (without reflector). This, once again, further demonstrates that the enhancements in IPCE found in the MDM system are attributed to the prolonged carrier's lifetime and the near-field enhancement as a consequence of mode coupling effect rather than merely the enhanced optical absorption, as the IQE is normalized to the number of absorbed photons. [43] Therefore, the superior performance of hot carrier generation in MDM55 can be attributed to the intense local electric field generated by the interplay of three modes under the strong coupling conditon.[44,45]

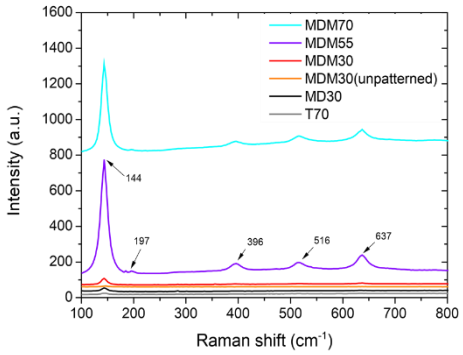

Fig. 4 The measured Raman spectra of the AuNHA/TiO_2/Au MDM absorbers with different TiO2 thicknesses. MD30 represents the absorbers without the back Au reflector, and T70 denotes the absorber with only a bare TiO_2 layer. They are used as controls.

Conclusion

This work has studied the relationship between the mode coupling effect of the AuNHA/TiO_2/Au MDM structure and the plasmon-induced hot carrier generation via an electrochemical system. With the change of the TiO_2 thickness in the MDM absorber, the three resonant modes present an anti-crossing behaviour and satisfy the strong coupling condition. For the MDM structures with different TiO_2 thicknesses, the IPCE

spectra follow the general trend of the absorption spectra. The optimal MDM absorber with the 55-nm TiO_2 layer produces the maximum IPCE of 1.5% and yields an enhanced photocurrent (enhanced by at least 1.26 times) as a result of the plasmon-induced hot carrier generation. The enhancement is attributed to the strong local field confined within the cavity by the mode hybridization as verified by both the SERS measurements and the FDTD simulations. This work presents a highly-efficient plasmonic absorber design, which may find potential applications in visible-light photocatalysis.

Experimental section

Sample fabrication

Prior to film deposition, the fluorine-doped tin oxide (FTO) glasses are pre-cleaned by ultrasonication sequentially in acetone, isopropanol, and DI water for 10 minutes each. They are then dried by pure nitrogen and treated by oxygen plasma (Harrick) to remove any residual organic substances on the substrates. The gold back reflector is deposited onto the FTO glasses by magnetron sputtering deposition (Denton). Before the deposition, the chamber is evacuated by a cryopump until the base pressure reached below 9×10^{-7} Torr. Gold with purity of 99.99% is used as a target. During the deposition, sputtering power of 80W and argon flow of 30 sccm is maintained. TiO_2 film is deposited onto the gold reflectors or the FTO substrates by atomic layer deposition (ALD) (Ultratech). Chemical precursor with Ti and H_2O are introduced alternately into the chamber in each cycle. The ALD process is implemented at 150 ^oC and the deposition rate is found to be 0.47 Å per cycle. After the deposition, the samples with TiO_2 thin film are then annealed in air for 1 hour at 400 ^oC to transform the TiO_2 from amorphous to anatase phase. Au nanohole array is fabricated by NSL and the RIE process. The polystyrene nanosphere with 10% solid suspended in DI water is purchased from the market. The suspension is then diluted with 1:1 v% absolute ethanol and dispersed by ultrasonication every time before use. The detailed procedure of NSL can be found in other literatures.[46,47] In brief, 20 µl polystyrene nanosphere suspension is added dropwise onto the water surface of a reservoir. Subsequently, few drops of sodium dodecyl sulfate (SDS) are added to reduce the surface tension of water. To obtain high quality closely-packed nanosphere template, the hydrophilicity of the substrate is crucial. Thus, the as-deposited TiO_2 films are treated by oxygen plasma (Harrick) for 2 min to increase the hydrophilicity of the surface. The closely-packed nanospheres are carefully transferred from the water surface onto the as-deposited TiO_2 films and are then left to dry naturally. To fabricate the evaporation mask for nanohole array, the closely-packed nanospheres on TiO_2 film are etched isotropically by Oxygen RIE technique (Trion). During etching process, the flow of purging O_2, working pressure, and RIE power are set at 30 sccm, 250 mTorr and 80 W, respectively. The etching rate is about 1.2 nm/s as confirmed by the SEM images. The resultant etched nanospheres are then used as the evaporation mask to fabricate the AuNHAs by the electron beam evaporation (Denton). Gold pellets with purity of 99.99% are used as an evaporation source. The evaporation is conducted until the base pressure of the chamber is reached below 9×10^{-7} Torr. During the deposition, the substrate holder is rotated at a constant rate of 20 r.p.m. to ensure the film uniformity. The deposition rate and the thickness are controlled by a quartz crystal monitor (INFICON). The deposition rate is maintained at 0.5 Å/s to retain good adhesion, good control of thickness and low roughness. The AuNHA pattern is finally obtained after the lift-off of the nanosphere template by ultrasonic bath in toluene.

Characterization

The morphology of nanostructures is studied by images acquired by the field emission scanning electron microscope (FESEM) (JEOL). The reflection spectra of samples are measured by the UV-visible spectrometer coupled with an integrating sphere (PerkinElmer). Both the scattering and the specular reflection signal are recorded inside the integrating sphere for non-transparent samples in a single measurement. Therefore, the absorption spectrum A can be calculated as $A(\lambda)= 1 - R(\lambda)$, where R represents the reflection spectrum.

Numerical simulation

The theoretical calculation of far-field and near-field spectra is performed by Finite-Difference Time-Domain (FDTD) software (Lumerical). To simulate the structures with nanohole array, a unit cell with the periodic boundaries in the x- and y-directions is implemented. A plane-wave source is injected from the air side to the structure. For the simulations involving the time-averaging or wavelength dependent spectra, Fourier transform monitors are employed. Since the scattered light can be fully recorded by a 2D monitor, the absorption, A, of the structures is generally defined as $A(\lambda)= 1 - R(\lambda) - T(\lambda)$, here R is the reflection, and T the transmission. Override mesh with the size of 0.8 nm is established near the nano-patterns and convergence testing is conducted to ensure the precision of simulation. The dielectric functions of Au, SiO_2, and TiO_2 used for the simulation are adopted from literatures.[48-50]

Photoelectrochemical measurements

The photocurrent is measured by the three-electrode configuration electrochemical cell. The testing samples, the platinum wire, and the saturated calomel electrode (SCE) are used as the working electrode, the counter electrode, and the reference electrode, respectively. Three electrodes are connected to an electrochemical station for characterization. The electrolyte solution used in this work contains 2.5 mM $Fe_2(SO_4)_3$, 10 mM $FeSO_4$, and 0.5 M Na_2SO_4. For the measurement of current generation by the broadband light, a xenon light source of 150 W equipped with a 490-nm long-pass filter is used. In the IPCE measurement, band pass filters are coupled with the 150 W xenon light source. The IPCE is calculated by

$$IPCE(\lambda) = \frac{1240 \cdot I\left(\mathrm{A/cm^2}\right)}{\lambda(\mathrm{nm}) \cdot P\left(\mathrm{W/cm^2}\right)}$$

, where I and P are the photocurrent density and the optical power of the source, respectively. The optical power of monochromatic light is measured by a handheld power meter (ThorLab). All the photocurrent signals in this work are measured under the bias of 0.5 V vs. SCE.

Raman spectra measurements

All the Raman spectra are measured by a commercial confocal Raman spectrometer (alpha300, WITec). Two laser sources of wavelength (532 nm and 633 nm), a monochromator, and a Peltier cooled CCD unit are integrated into a single spectrometer. All the spectra are measured as a function of Raman shift. The characterization of the samples with TiO_2 is done by the laser source with the wavelength of 633 nm, optical power of 1 mW and in the spectral range 100 – 900 cm^{-1}.

Conflicts of interest

There are no conflicts to declare.

Acknowledgements

This work is supported by the Research Grants Council of Hong Kong (152184/15E, 152127/17E, 152126/18E, 152219/19E, 152156/20E, 15304519 and N_PolyU511/20), The Hong Kong Polytechnic University (1-ZE14, 1-ZE27 and 1-ZVGH), The City University of Hong Kong (9610434). The technical assistance and facility support from Materials Research Centre and from the University Research Facility in Material Characterization and Device Fabrication of The Hong Kong Polytechnic University are acknowledged.

References

1 M. Pelton and G. W. Bryant, *Introduction to metal-nanoparticle plasmonics*, John Wiley & Sons, 2013.
2 B. Ai, Z. Wang, H. Moehwald and G. Zhang, *ACS Nano*, 2017, **11**, 12094-12102.
3 J. T. Li, S. K. Cushing, P. Zheng, F. K. Meng, D. Chu and N. Q. Wu, *Nat. Commun.*, 2013, **4**.
4 D. Tordera, D. Zhao, A. V. Volkov, X. Crispin and M. P. Jonsson, *Nano Lett.*, 2017, **17**, 3145-3151.
5 J. Braun, B. Gompf, G. Kobiela and M. Dressel, *Phys. Rev. Lett.*, 2009, **103**.
6 M. Liu, Y. Song, Y. Zhang, X. Wang and C. Jin, *Plasmonics*, 2012, **7**, 397-410.
7 Q. Li, Z. Li, X. Wang, T. Wang, H. Liu, H. Yang, Y. Gong and J. Gao, *Nanoscale*, 2018, **10**, 19117-19124.
8 Q. Li, Z. Z. Li, H. G. Yang, H. Liu, X. Y. Wang, J. S. Gao and J. L. Zhao, *Opt. Exp.*, 2016, **24**, 25885-25893.
9 Q. Shi, T. U. Connell, Q. Xiao, A. S. R. Chesman, W. Cheng, A. Roberts, T. J. Davis and D. E. Gomez, *ACS Photonics*, 2019, **6**, 314-321.
10 E. S. H. Kang, S. Chen, S. Sardar, D. Tordera, N. Armakavicius, V. Darakchieva, T. Shegai and M. P. Jonsson, *ACS Photonics*, 2018, **5**, 4046-4055.
11 J. H. Yang, Q. Sun, K. Ueno, X. Shi, T. Oshikiri, H. Misawa and Q. H. Gong, *Nat. Commun.*, 2018, **9**, 8.
12 S. Savasta, R. Saija, A. Ridolfo, O. Di Stefano, P. Denti and F. Borghese, *ACS Nano*, 2010, **4**, 6369-6376.
13 K. Hennessy, A. Badolato, M. Winger, D. Gerace, M. Atature, S. Gulde, S. Falt, E. L. Hu and A. Imamoglu, *Nature*, 2007, **445**, 896-899.
14 M. L. Brongersma, N. J. Halas and P. Nordlander, *Nat. Nanotechnol.*, 2015, **10**, 25-34.
15 X. Zhang, Y. L. Chen, R.-S. Liu and D. P. Tsai, *Rep. Prog. Phys.*, 2013, **76**.
16 M. W. Knight, H. Sobhani, P. Nordlander and N. J. Halas, *Science*, 2011, **332**, 702-704.
17 X. Shi, K. Ueno, T. Oshikiri, Q. Sun, K. Sasaki and H. Misawa, *Nat. Nanotechnol.*, 2018, **13**, 953-+.
18 Y. F. Cao, T. Oshikiri, X. Shi, K. Ueno, J. Li and H. Misawa, *ChemNanoMat*, 2019, **5**, 1008-1014.
19 H. Y. Shan, Y. Yu, X. L. Wang, Y. Luo, S. Zu, B. W. Du, T. Y. Han, B. W. Li, Y. Li, J. R. Wu, F. Lin, K. B. Shi, B. K. Tay, Z. Liu, X. Zhu and Z. Y. Fang, *Light Sci. Appl.*, 2019, **8**.
20 J. Jung, T. Sondergaard and S. I. Bozhevolnyi, *Phys. Rev. B*, 2009, **79**.
21 H. Dotan, O. Kfir, E. Sharlin, O. Blank, M. Gross, I. Dumchin, G. Ankonina and A. Rothschild, *Nat. Mater.*, 2013, **12**, 158-164.
22 M. A. Kats, R. Blanchard, S. Ramanathan and F. Capasso, *Opt. and Photonics News*, 2014, **25**, 40-47.
23 S. I. Bozhevolnyi, V. S. Volkov, E. Devaux, J. Y. Laluet and T. W. Ebbesen, *Nature*, 2006, **440**, 508-511.
24 S. A. Maier, *Plasmonics: fundamentals and applications*, Springer Science & Business Media, 2007.
25 E. J. C. Dias and F. J. G. de Abajo, *ACS Nano*, 2019, **13**, 5184-5197.
26 C. Genet and T. W. Ebbesen, *Nature*, 2007, **445**, 39-46.
27 J. A. Dionne, L. A. Sweatlock, H. A. Atwater and A. Polman, *Phys. Rev. B*, 2006, **73**.
28 F. Yang, J. Sambles and G. Bradberry, *Phys. Rev. B*, 1991, **44**, 5855.
29 G. C. Li, Y. L. Zhang, J. Jiang, Y. Luo and D. Y. Lei, *ACS Nano*, 2017, **11**, 3067-3080.
30 G. C. Li, Q. Zhang, S. A. Maier and D. Lei, *Nanophotonics*, 2018, **7**, 1865-1889.
31 A. Sobhani, A. Manjavacas, Y. Cao, M. J. McClain, F. Javier Garcia de Abajo, P. Nordlander and N. J. Halas, *Nano Lett.*, 2015, **15**, 6946-6951.
32 V. G. Kravets, A. V. Kabashin, W. L. Barnes and A. N. Grigorenko, *Chem. Rev.*, 2018, **118**, 5912-5951.
33 G. Khitrova, H. M. Gibbs, M. Kira, S. W. Koch and A. Scherer, *Nat. Phys.*, 2006, **2**, 81-90.
34 J. Cuadra, D. G. Baranov, M. Wersall, R. Verre, T. J. Antosiewicz and T. Shegai, *Nano Lett.*, 2018, **18**, 1777-1785.
35 N. Sakai, Y. Fujiwara, Y. Takahashi and T. Tatsuma, *Chemphyschem*, 2009, **10**, 766-769.
36 Y. Nishijima, K. Ueno, Y. Yokota, K. Murakoshi and H. Misawa, *J. Phys. Chem. Lett.*, 2010, **1**, 2031-2036.
37 K. Saito, I. Tanabe and T. Tatsuma, *J. Phys. Chem. Lett.*, 2016, **7**, 4363-4368.
38 E. Kazuma, N. Sakai and T. Tatsuma, *Chem. Commun.*, 2011, **47**, 5777-5779.
39 H. Lee, H. Lee and J. Y. Park, *Nano Lett.*, 2019, **19**, 891-896.
40 E. Cortes, W. Xie, J. Cambiasso, A. S. Jermyn, R. Sundararaman, P. Narang, S. Schlucker and S. A. Maier, *Nat. Commun.*, 2017, **8**.
41 D. Liu, T. Wu, Q. Zhang, X. Wang, X. Guo, Y. Su, Y. Zhu, M. Shao, H. Chen, Y. Luo and D. Lei, *Acs Nano*, 2019, **13**, 7644-7654.

42 W. F. Zhang, Y. L. He, M. S. Zhang, Z. Yin and Q. Chen, *J. Phys. D: Appl. Phys.*, 2000, **33**, 912-916.
43 G. Tagliabue, A. S. Jermyn, R. Sundararaman, A. J. Welch, J. S. DuChene, R. Pala, A. R. Davoyan, P. Narang and H. A. Atwater, *Nat. Commun.*, 2018, **9**, 8.
44 K. H. W. Ho, A. X. Shang, F. H. Shi, T. W. Lo, P. H. Yeung, Y. S. Yu, X. M. Zhang, K. Y. Wong and D. Y. Lei, *Adv. Funct. Mater.*, 2018, **28**.
45 D. C. Ratchford, A. D. Dunkelberger, I. Vurgaftman, J. C. Owrutsky and P. E. Pehrsson, *Nano Lett.*, 2017, **17**, 6047-6055.
46 P. Gao, J. He, S. Zhou, X. Yang, S. Li, J. Sheng, D. Wang, T. Yu, J. Ye and Y. Cui, *Nano Lett.*, 2015, **15**, 4591-4598.
47 H. Li, J. Low, K. S. Brown and N. Wu, *IEEE Sens. J.*, 2008, **8**, 880-884.
48 P. B. Johnson and R.-W. Christy, *Phys. Rev. B*, 1972, **6**, 4370.
49 E. D. Palik, *Handbook of optical constants of solids*, Academic press, 1998.
50 M. Hasan, A. Haseeb, R. Saidur and H. H. Masjuki, *Int. J. Chem. Biol. Eng.*, 2008, **1**, 92-96.

Supporting Information

Enhancing plasmonic hot carrier generation by strong coupling of multiple resonant modes

Yat Lam Wong, Huaping Jia, Aoqun Jian, Dangyuan Lei, Abdel I. El Abed, and Xuming Zhang[*]

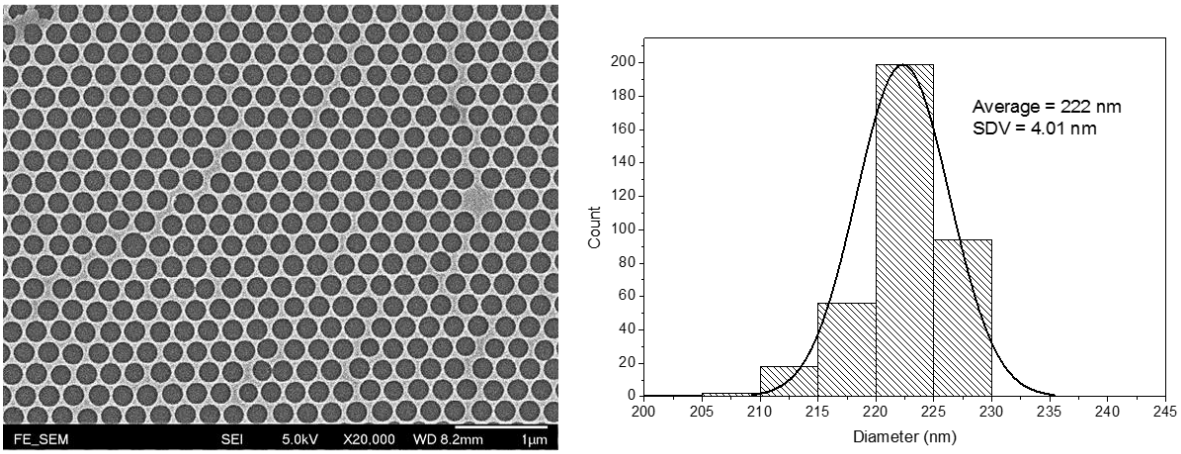

Fig. S1. The SEM image (left) and the distribution of the diameter of holes (right) extracted from the SEM image. The average and standard deviation of the holes‘ diamter are 222 nm and 4.01 nm, respectively.

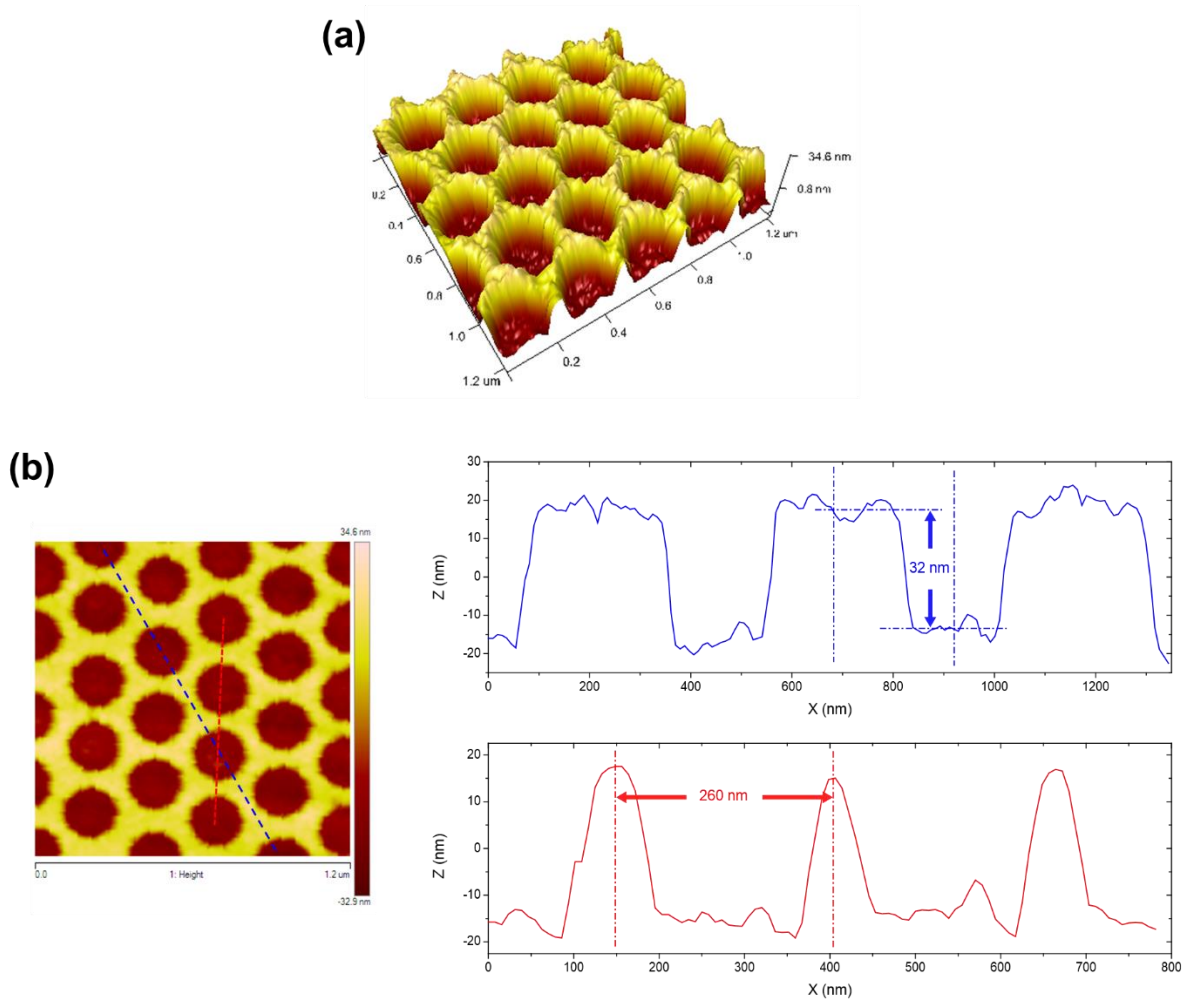

Fig. S2. The 3D AFM image of the AuNHA (a); and the top view and the profiles of along the blue and red dash lines (b).

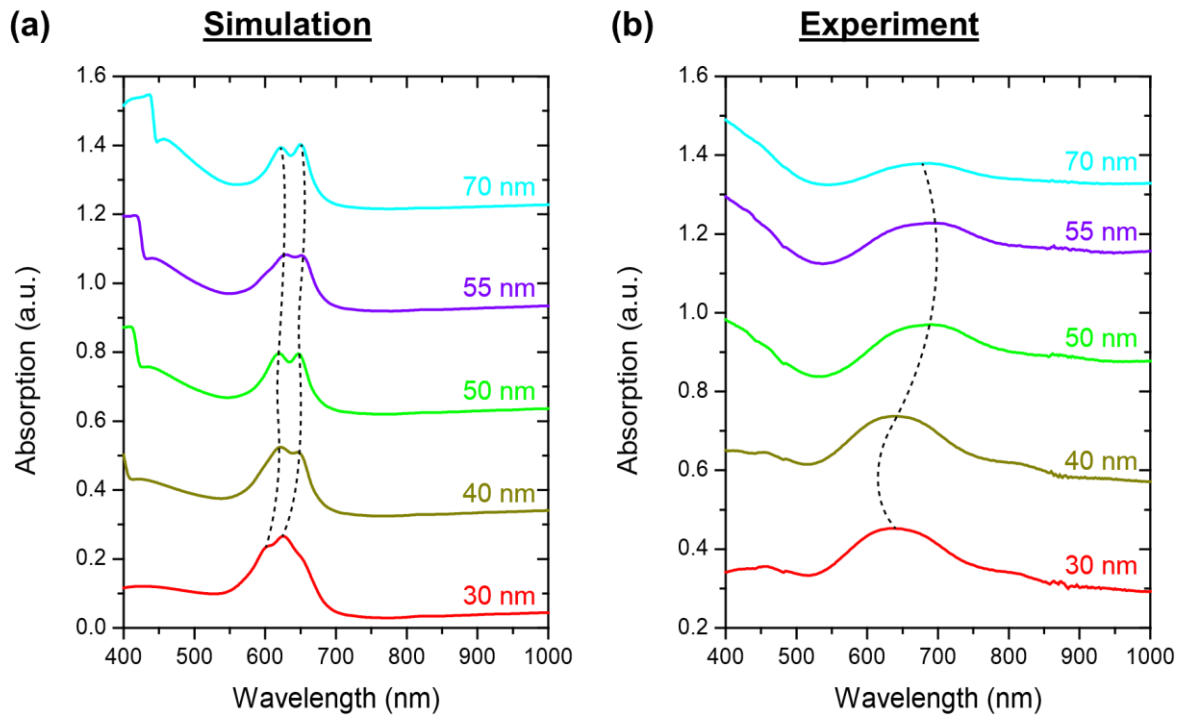

Fig. S3. The FDTD calculated (a) and experimental (b) absorption spectra of the AuNHA/TiO_2 metal-dielectric (MD) absorbers with the TiO_2 thicknesses of 30, 40, 50, 55, and 70 nm (from bottom to top).

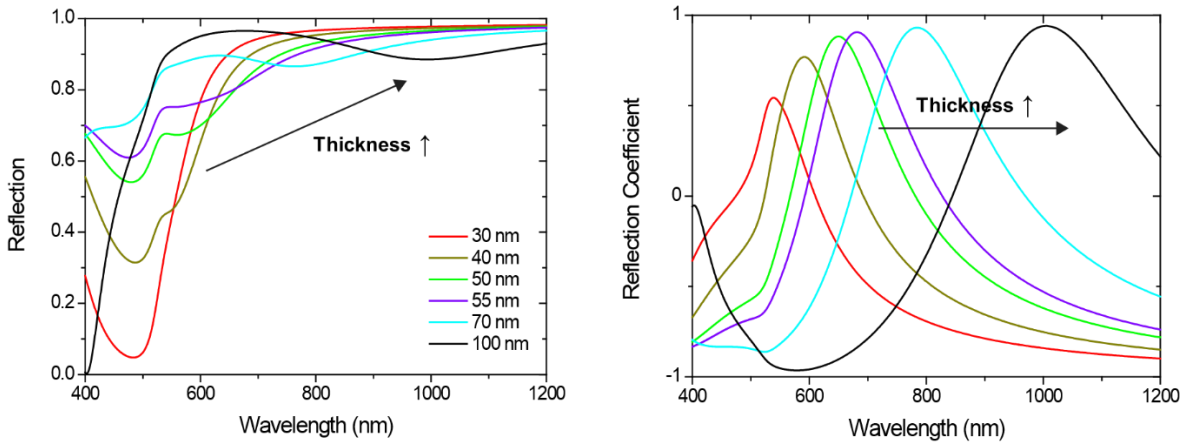

Fig. S4. The reflection spectra (left) and the associated reflection coefficient (right) of the TiO_2/Au/SiO_2 structure with different TiO_2 thicknesses.

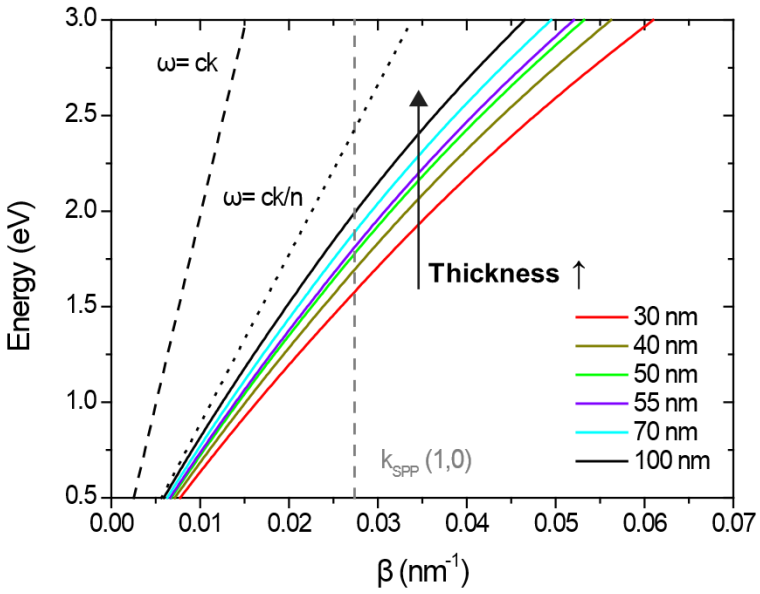

Fig. S5. The dispersion relation of the GSPP mode supported by the AuNHA/TiO_2/Au MDM structure with different thicknesses of TiO_2 layer. The black dashed line and the black dotted line represent the light lines in air and TiO_2, respectively. The gray dashed line represents the propagation constant of the GSPP confined in the structure excited by the grating coupled with the normal incident light.

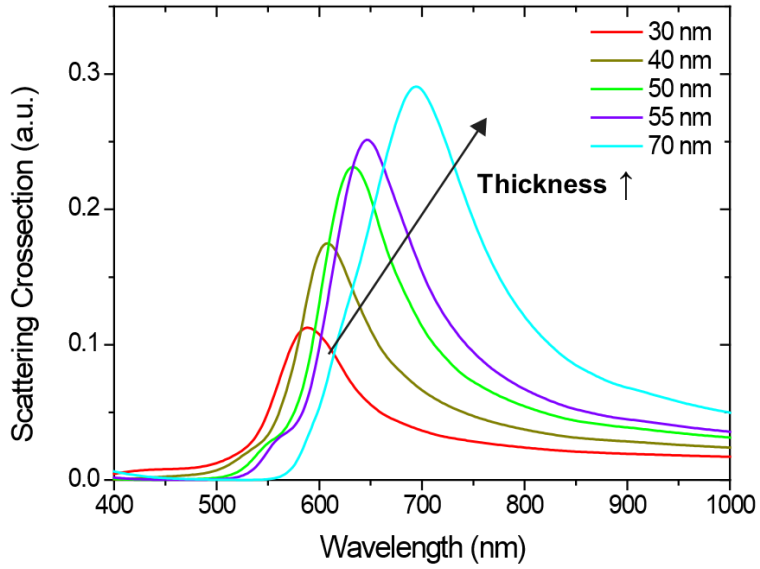

Fig. S6. The FDTD-calculated scattering cross-section spectra of the MDM structure that has a top Au film perforated with a single hole of diameter 220 nm, a middle TiO_2 layer and an Au back reflector. The peak position is gradually redshifted with the increase of TiO_2 thickness.

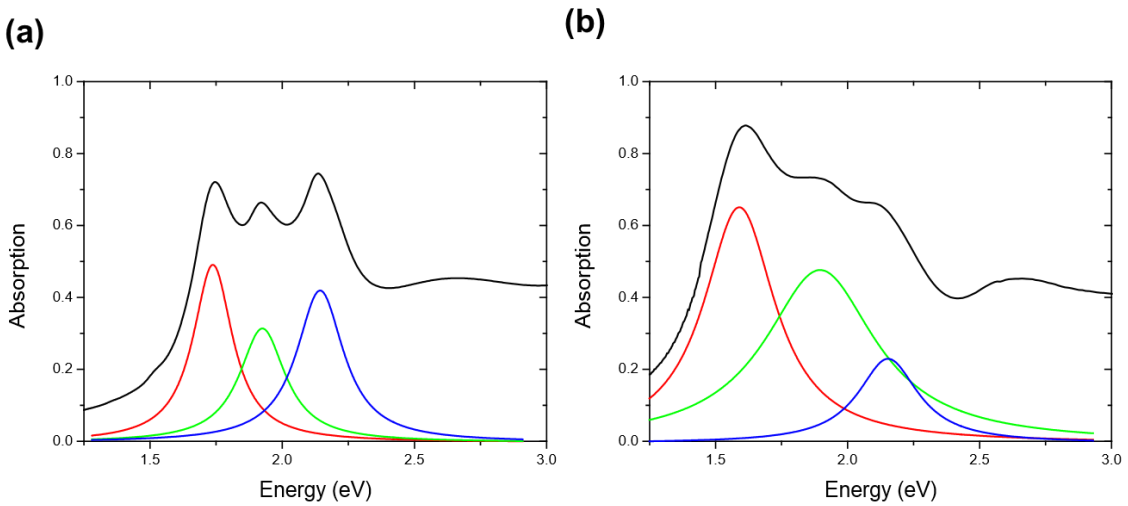

Fig. S7. The FDTD-calculated (a) and experimental (b) absorption spectra of the AuNHA/TiO_2/Au MDM absorber with the TiO_2 thickness of 55 nm. The color curves represent the Lorentzian fits of the resonances.

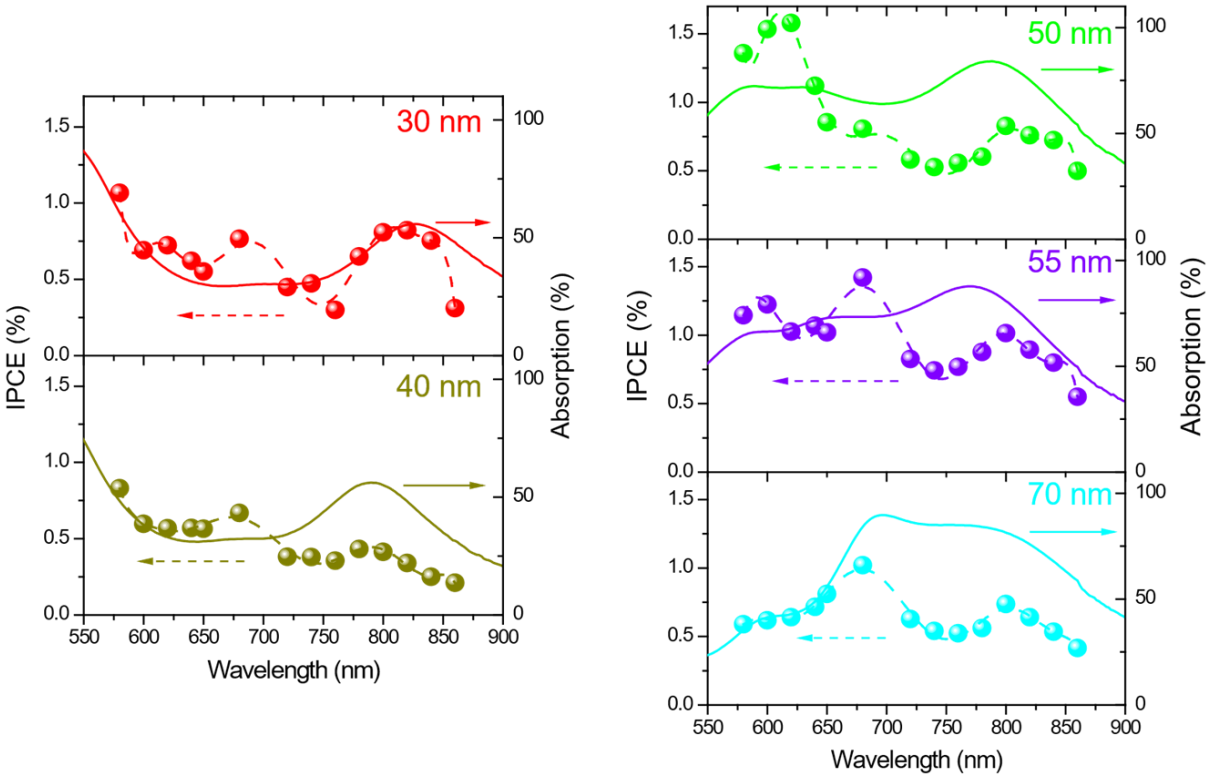

Fig. S8. The IPCE spectra (left axis) and the absorption spectra (right axis) of the MDM structure with varying thickness of TiO_2. All the photocurrents generated by the absorbers are measured under the bias voltage of 0.5 V vs. SCE.

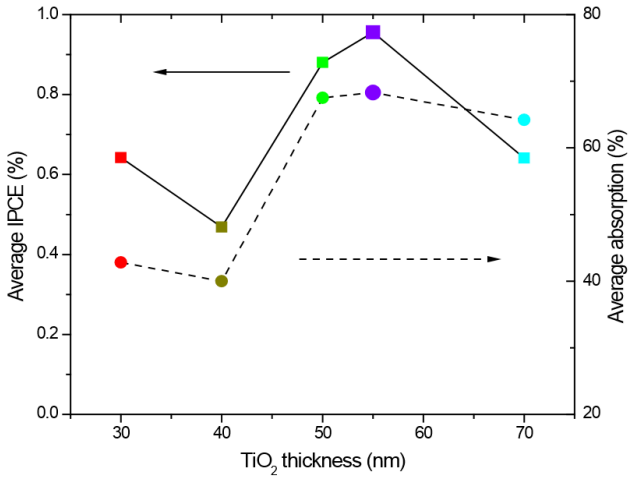

Fig. S9. The average IPCE (left) and the average optical absorption (right) of the MDM absorber with varying thickness of TiO_2 over the measurement range from 580 to 860 nm.

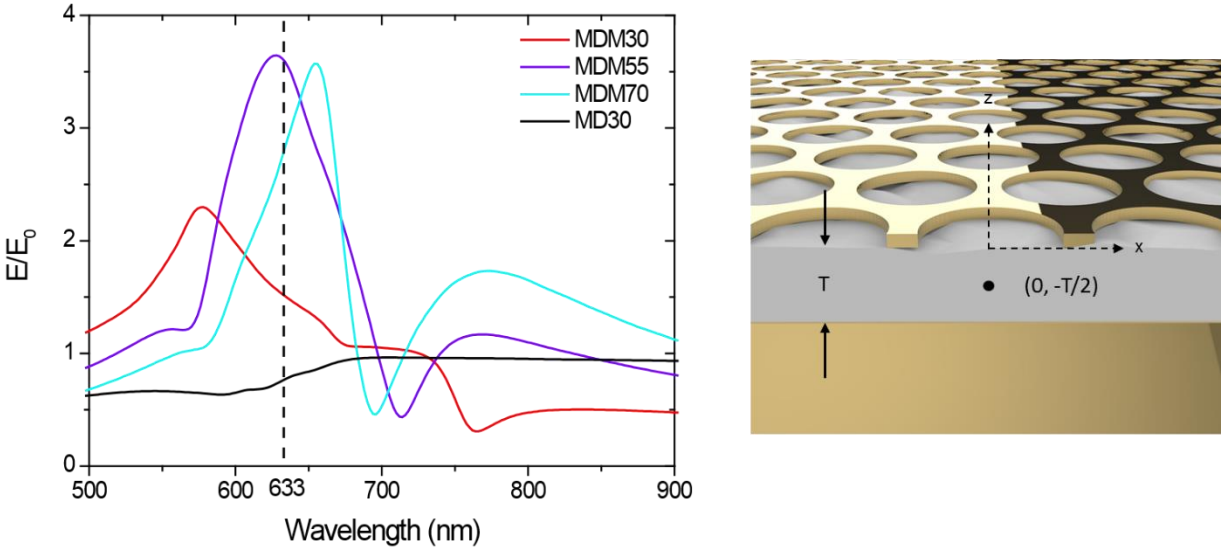

Fig. S10. The FDTD-calculated local electric field spectra of four different structures (i.e., three MDM absorbers with different TiO_2 thicknesses and one MD structure without the back reflector). The observation point is located at the middle of the TiO_2 below the center of the hole. The dashed line represents the wavelength of the laser source of the SERS.

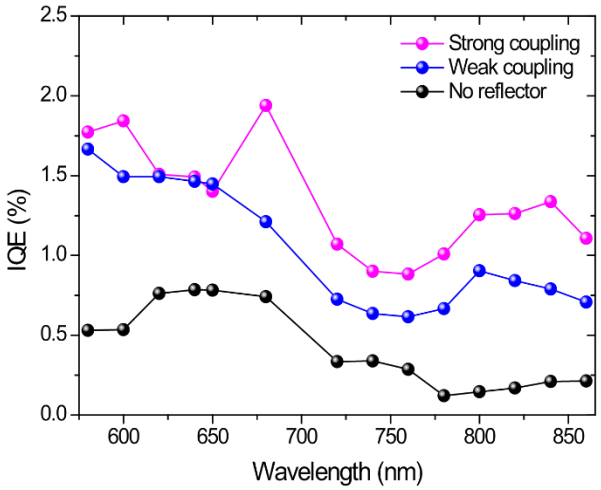

Fig. S11. The interrnal quantum efficiency (IQE) spectra of the MDM structure that fulfills the strong coupllng condtion (magenta), the MDM structure that fail to fulfill the strong coupling condition (blue), and the MD structure that does not support any mode coupling effect (black). The IQE is calculated by deviding the IPCE by the opctical absorption of the absortber.

Supporting discussion:

1. Gap surface plasmon polariton (GSPP) mode

The dispersion relation of all SPR modes in the system with a dielectric film of thickness *d* sandwiched by two metallic films of thickness h can be implicitly expressed by the following expression [S1, S2]

$$\frac{\left(\frac{k_2}{\varepsilon_{m1}}-\frac{k_3}{\varepsilon_d}\right)\left(\frac{k_1}{\varepsilon_1}+\frac{k_2}{\varepsilon_{m1}}\right)e^{k_2 h}e^{-\frac{k_3 d}{2}}+\left(\frac{k_2}{\varepsilon_{m1}}-\frac{k_3}{\varepsilon_d}\right)\left(\frac{k_1}{\varepsilon_1}-\frac{k_2}{\varepsilon_{m1}}\right)e^{-k_2 h}e^{-\frac{k_3 d}{2}}}{\left(\frac{k_2}{\varepsilon_{m1}}+\frac{k_3}{\varepsilon_d}\right)\left(\frac{k_1}{\varepsilon_1}+\frac{k_2}{\varepsilon_{m1}}\right)e^{k_2 h}e^{\frac{k_3 d}{2}}+\left(\frac{k_2}{\varepsilon_{m1}}-\frac{k_3}{\varepsilon_d}\right)\left(\frac{k_1}{\varepsilon_1}-\frac{k_2}{\varepsilon_{m1}}\right)e^{-k_2 h}e^{\frac{k_3 d}{2}}}$$
$$-\frac{\left(\frac{k_4}{\varepsilon_{m2}}-\frac{k_3}{\varepsilon_d}\right)\left(\frac{k_5}{\varepsilon_2}-\frac{k_4}{\varepsilon_{m2}}\right)e^{-k_4 h}e^{\frac{k_3 d}{2}}+\left(\frac{k_4}{\varepsilon_{m2}}+\frac{k_3}{\varepsilon_d}\right)\left(\frac{k_4}{\varepsilon_{m2}}+\frac{k_5}{\varepsilon_2}\right)e^{k_4 h}e^{\frac{k_3 d}{2}}}{\left(\frac{k_4}{\varepsilon_{m2}}+\frac{k_3}{\varepsilon_d}\right)\left(\frac{k_5}{\varepsilon_2}-\frac{k_4}{\varepsilon_{m2}}\right)e^{-k_4 h}e^{-\frac{k_3 d}{2}}+\left(\frac{k_4}{\varepsilon_{m2}}-\frac{k_3}{\varepsilon_d}\right)\left(\frac{k_4}{\varepsilon_{m1}}+\frac{k_5}{\varepsilon_2}\right)e^{k_4 h}e^{-\frac{k_3 d}{2}}}$$
$$=0$$

, and - (S1)

, where the subscripts 1, 2, 3, 4, and 5 represent the media where the light transmitted sequentially, namely vacuum, Au, TiO_2, Au, and SiO_2 respectively (schematically shown in fig. S11); β_j refers to the propagation constant in medium j. The dispersion relations of the internal GSPP mode for different thickness of TiO_2 are calculated by the above equation and presented in fig. S5. Of course, the GSPP mode cannot be coupled from free space light without the assistance of a grating or scatterers as the light lines in fig. S5 never cross the dispersion curves. For normal incident light, the GSPP excited by the grating coupling effect provided by an NHA ordered in a hexagonal lattice should obey the conservation of momentum [S3], such that

$$\beta_{GSPP} = \frac{2\pi}{P}\sqrt{\frac{4}{3}(i^2 + i \cdot j + j^2)} \quad \text{(S2)}$$

, where P is the periodicity of the NHA; i and j are the scattering orders of the NHA. The line associated with lowest grating order, namely (1, 0), is calculated and plotted in fig. S5.

In order to have a better understanding on the GSPP supported by the proposed structure, a structure with only a few holes arranged in the short-range ordered lattice, as shown in fig. S11, are investigated via FDTD. One of the advantages of studying short range ordered structures is the possibility of observing the undisturbed propagating modes. The calculated absorption spectra of the MDM absorbers with 7 holes and 19 holes are presented in fig. S12. For the structures with short range ordered, three peaks which are previously observed in the structure with AuNHA are also discernable at the same spectral positions. The peak with lowest energy for the structure of TiO_2 thickness of 55 nm corresponds to the GSPP mode, which the wavelength dependent z-component electric field distribution of the structure at 710 nm can directly identify the GSPP mode propagating in the TiO_2 film as positive and negative fields alternatingly distribute along the layer (see fig. S13). Through the time evolution of E_z field shown in fig. S14, it clearly visualizes the propagation of the GSPP mode. For instance, the

LSPR mode of the holes are excited at the beginning and then it is coupled to the GSPP which is confined within two metallic films and guided in the TiO_2 layer. We further analyze the field distribution of an arbitrary maximum shown in fig. S13, and plot against the z position (see fig. S15), the symmetric distribution of the field across the AuNHA/TiO_2 and TiO_2/Au interfaces indicates that the corresponding GSPP mode is a long range guiding mode [S4].

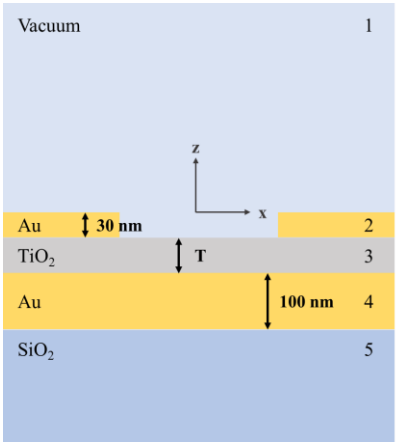

Fig. S11. The schematic diagram of the layer structure in which the calculation in Equation (S1) is implemented.

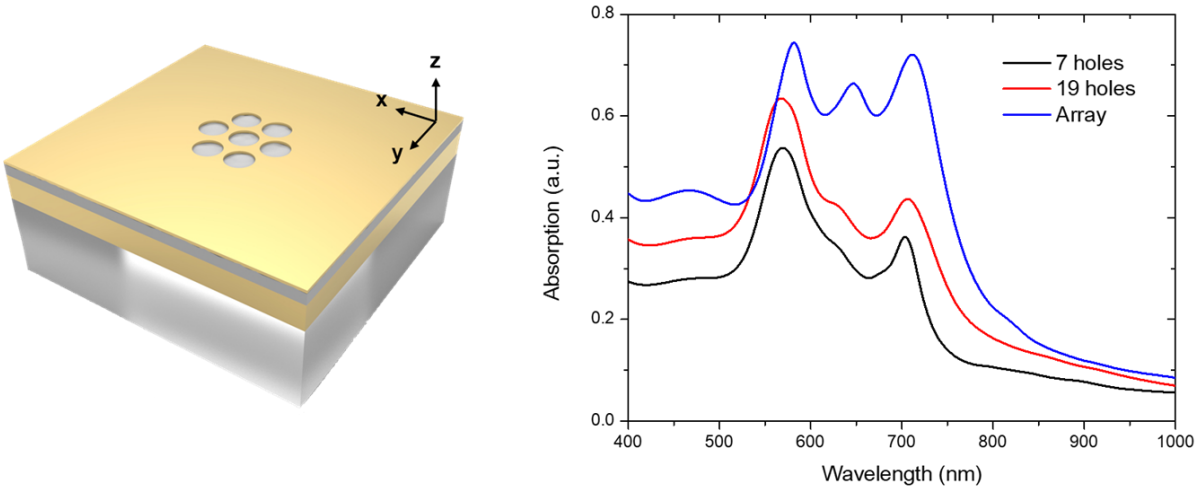

Fig. S12. The schematic diagram of the nonperiodic, hexagonally arranged nanoholes (left) and the corresponding calculated absorption spectra (right). The absorption spectrum of the MDM structure with AuNHA is plotted in the figure (blue curve) for reference.

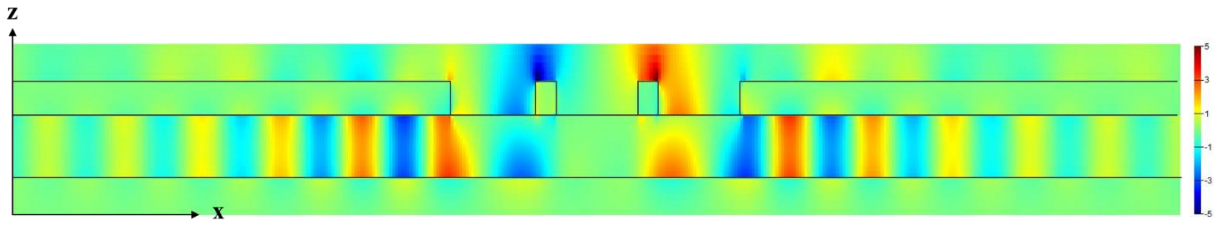

Fig. S13. The E_z distribution of the MDM absorber with 7 nonperiodic nanoholes and TiO_2 thickness of 55 nm at the resonance wavelength of 710 nm. The color bar in the diagram from red to green to blue represents the polarity and intensity of the field.

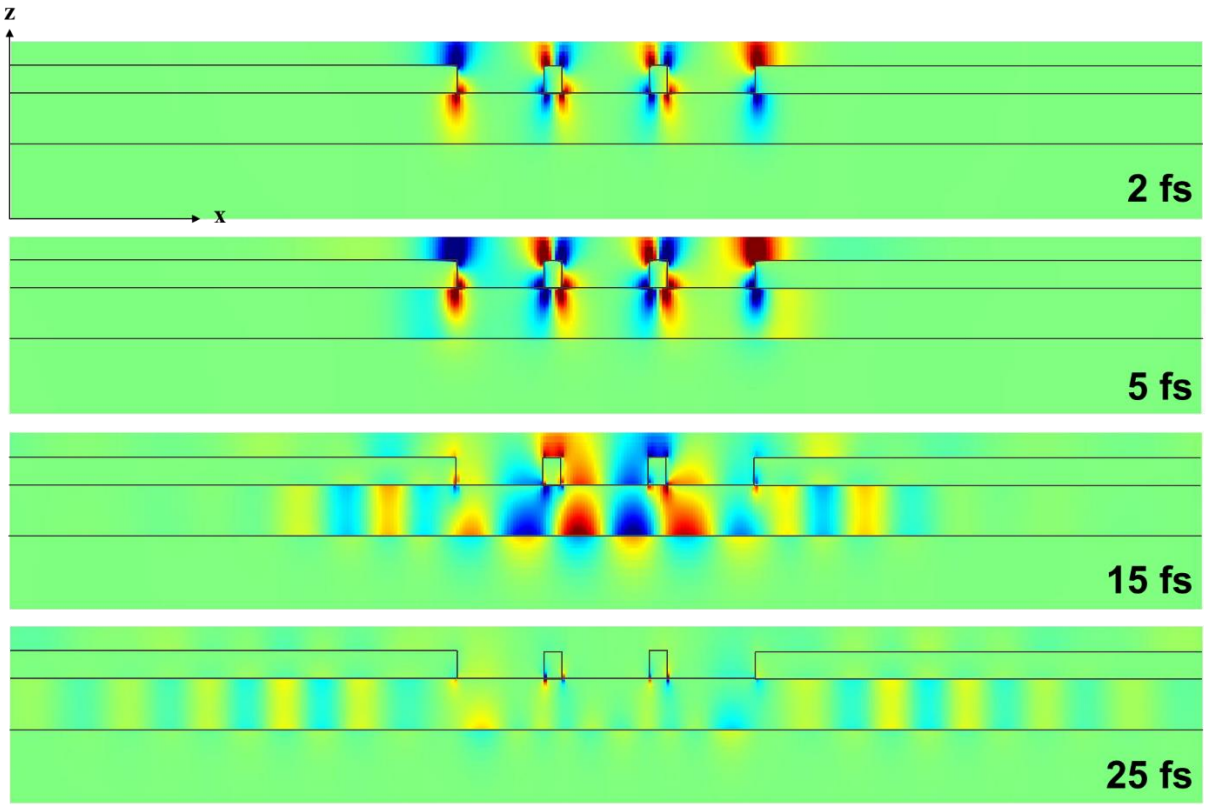

Fig. S14. The time domain E_z field distribution on the xz plane located at y = 0 nm at the time 2, 5, 15, and 25 fs after the start of the simulation. The color in the diagrams represents the same polarity as shown in the color bar in fig. S13.

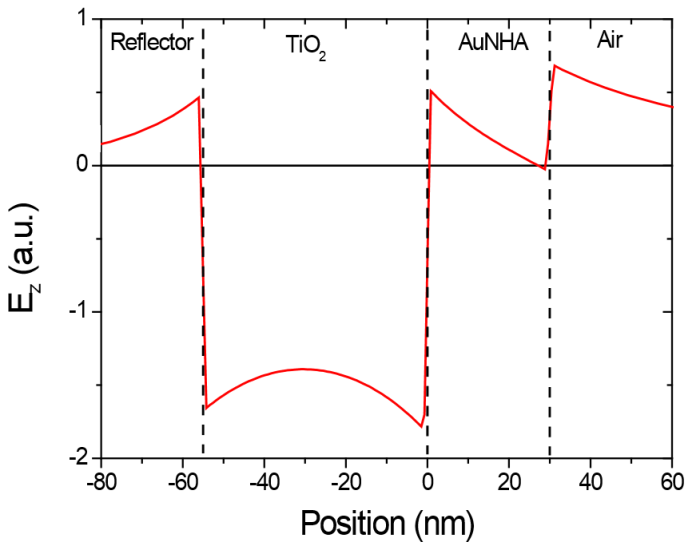

Fig. S15. The intensity of E_z as a function of z position at an arbitrary maximum shown in fig. S13 at the resonance wavelength of 710 nm.

References

1. R. Ortuno, C. Garcia-Meca, F. J. Rodriguez-Fortuno, J. Marti and A. Martinez, *Phys. Rev. B*, 2009, **79**.
2. E. Economou, *Phys. Rev.*, 1969, **182**, 539.
3. Q. Li, Z. Li, X. Wang, T. Wang, H. Liu, H. Yang, Y. Gong and J. Gao, *Nanoscale*, 2018, **10**, 19117-19124.
4. P. Berini, *Opt. Exp.*, 2006, **14**, 13030-13042.